Topographic Reconstruction of the "Tianwen-1" Landing Area on the Mars Using High Resolution Imaging Camera Images

Wei Yan, Xin Ren, Jianjun Liu, Li Zhang, Wangli Chen, Dong Wang, Qiang Fu, Xu Tan, Xiaoxia Zhang, Haibin Ai, Baoqian Wang, Quanquan Zhi, Zichen Huang, and Chen Song

***Abstract*— High-resolution optical cameras have always been important scientific payloads in Mars exploration missions, and the Mars topographic data produced by their detection data can provide support for scientific research on Mars geomorphology and geological structure evolution. As of December 2021, there are still relatively few high-resolution image data at the submeter level on the Martian surface, with about 2.6% global coverage and even more limited stereo coverage (just about 0.4%). At the same time, there are still some difficulties in data acquisition and terrain reconstruction processing methods for high-resolution Mars images that need to be solved. This article described how we designed the in-orbit stereo imaging strategy based on the characteristics of the high-resolution imaging camera (HiRIC) of China's first Mars exploration mission (Tianwen-1), studied the technical solutions for HiRIC stereo image photogrammetry processing, and produced a topographic dataset for the "Tianwen-1" landing area, including a digital orthophoto map (DOM) with a ground sample distance (GSD) of 0.7 and 3.5 m and a digital elevation model (DEM) with a GSD of 3.5 m. Precision analysis results show that these topographic data have good consistency in planar position and elevation compared with the existing Mars terrain data and have advantages in spatial resolution and terrain detail expression, which will be widely used in the geological background study of the "Tianwen-1" landing area, as well as landing site positioning, Martian surface remote operation planning, and other Mars scientific research and engineering tasks.**

***Index Terms*— Digital topographic models, high-resolution imaging camera (HiRIC), photogrammetry, stereo imaging, Tianwen-1, topographic dataset.**

Manuscript received 30 March 2022; revised 30 July 2022; accepted 25 August 2022. Date of publication 15 September 2022; date of current version 30 September 2022. This work was supported by the Key Program of the Chinese Academy of Sciences under Grant ZDBS-SSW-TLC001. *(Corresponding authors: Xin Ren; Li Zhang.)*

Wei Yan, Xin Ren, and Jianjun Liu are with the Key Laboratory of Lunar and Deep Space Exploration, National Astronomical Observatories, Chinese Academy of Sciences, Beijing 100101, China, and also with the School of Astronomy and Space Science, University of Chinese Academy of Sciences, Beijing 100049, China (e-mail: renx@nao.cas.cn).

Li Zhang, Haibin Ai, and Baoqian Wang are with the Chinese Academy of Surveying and Mapping, Beijing 100036, China (e-mail: zhangl@casm.ac.cn).

Wangli Chen, Qiang Fu, Xu Tan, and Xiaoxia Zhang are with the Key Laboratory of Lunar and Deep Space Exploration, National Astronomical Observatories, Chinese Academy of Sciences, Beijing 100101, China.

Dong Wang is with the Changchun Institute of Optics, Fine Mechanics and Physics, Chinese Academy of Sciences, Changchun 130033, China.

Quanquan Zhi, Zichen Huang, and Chen Song are with the Beijing Aerospace Control Center, Beijing 100089, China.

Digital Object Identifier 10.1109/TGRS.2022.3206961

I. Introduction

MARS topographic information is the most important data to quantitatively describe the basic characteristics of the Martian surface, and it is indispensable for scientific research on surface topography, mineral and rock distribution, geological structure and evolution, gravity field and internal structure, atmospheric dynamics, and so on. At the same time, the high-precision topographic data can also support engineering tasks, such as probe orbit optimization design, landing site positioning, Mars rover exploration path planning, and so on. Therefore, the detailed reconstruction of Mars terrain is an important and fundamental work in Mars exploration missions.

High-resolution satellite images and laser altimeter have been two major categories of datasets for topographic modeling. To date, international Mars exploration missions have carried a variety of high-resolution optical cameras and laser altimeters, such as the Mars orbiter camera (MOC) [27], [29] and the Mars orbiter laser altimeter (MOLA) [39] on Mars global surveyor (MGS), the high-resolution imaging science experiment (HiRISE) [30] and context camera (CTX) [28] on Mars reconnaissance orbiter (MRO), the high-resolution stereo camera (HRSC) [15], [34] on Mars express, the color and stereo surface imaging system (CaSSIS) [42] on ExoMars trace gas orbiter (TGO), and so on. The images and detection data acquired by these payloads have been used to produce a rich set of mosaics and topographic data of the Mars [3], [16], [29], [31], [33], [35], [39], [43], which accurately characterize the topography of the Martian surface and provide a geographic benchmark for Mars exploration missions, exploration data processing, applications, and comprehensive scientific research.

In terms of technical characteristics, laser altimeter has a remarkable higher vertical accuracy and global consistency, allowing direct access to topographic information on the Martian surface; however, in the horizontal direction, the strip-like arrangement of points in widely spaced profiles suffers from severe differences of density, which reduce the effective resolution. The current "gold standard" for Martian topographic data, MOLA, has collected data globally with astonishingly high accuracy, but the sample spacing of this dataset is only about 300-m along track, and, in many places near the equator, adjacent MOLA ground tracks are separated by gaps of one to several kilometers [39]. In contrast, images

can provide much better horizontal resolution of terrain details, but photogrammetric processing of images requires stereo coverage of the Martian surface, as well as image enhancement, platform attitude high-frequency vibration elimination, and other processing to ensure the image quality. In addition, there are no absolute control points on the Martian surface, and the positional accuracy of image-based reconstructions of the Martian terrain depends entirely on the measurement accuracy of the probe's orbit and attitude data [10], [12], [20], [22], [23]. While techniques, such as 2-D photoclinometry or shape from shading, can be used to produce digital elevation models (DEMs) at the pixel resolution from single image, greatly optimizing the existing DEM spatial resolution (typically 10–20 times the image resolution for true resolution [24]), calibration against topographic data from another source is necessary to obtain an accurate, quantitative product. So, in practice, stereo coverage images are still needed [21].

It can be seen that each of these two datasets has its own advantages in generating Mars topographic data. Currently, the trend of most existing topographic data is to focus on the integration of different data sources, such as different images, different sensors, and different modes [1], [2], [6], [8], [10], [11], [17], [20], [22], [38], [46], which effectively optimizes the spatial resolution and absolute positioning accuracy of Mars topographic data in global and local regions. However, due to factors, such as differences in payload specifications, the complexity of photogrammetric processing, and so on, there is almost no standard technical solution for all Mars high-resolution image data processing currently. There are also still some outstanding problems need to fulfill for Mars images, such as the single texture of some images, image deformation caused by the high-frequency vibration in the platform pointing parameters, and so on, which seriously affect the image quality and the matching accuracy of images. In addition, the submeter-scale high-resolution image data of the Martian surface are still relatively small, the global coverage is about 2.6% (as of December 2021), and stereo coverage is even more limited, resulting in the lack of calibration data and control reference for high-resolution topographic data, which affects their absolute positioning accuracy. Therefore, it is of great importance to further study the reconstruction methods of detailed topographic data on the Martian surface and to integrate the existing images and topographic data to produce Mars topographic data with high spatial resolution and absolute positioning accuracy.

China's first Mars exploration mission (Tianwen-1) has been successfully launched an orbiter and a rover (named Zhurong) in July 2020. To date, "Tianwen-1" has successfully completed the scientific exploration missions in the Mars parking orbit and relay and survey orbit and entered the global reconnaissance orbit to carry out comprehensive remote sensing exploration of Mars [25]. The high-resolution imaging camera (HiRIC) is one of the scientific payloads on the "Tianwen-1" orbiter, which is used to obtain detailed optical images of interest areas on the Martian surface to study the surface topography and changes of the Mars, the identification of characteristic geomorphic units, as well as geological structure, such as landform of water, volcano, impact crater, erosion,

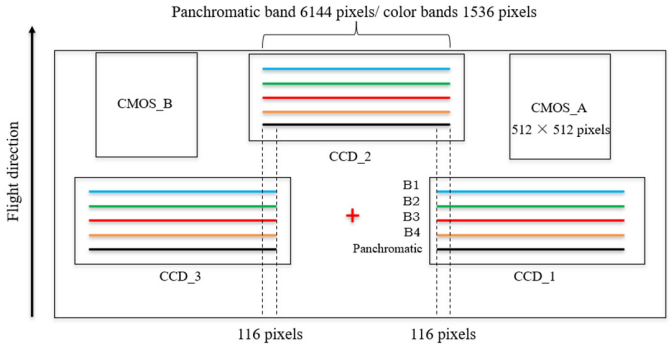

Fig. 1. Distribution of HiRIC CCDs and CMOS detectors on the focal plane. The probe flight direction is from the FOV of −0.1° to +0.535°, and the TDI CCD integral direction is from the blue imaging area (B1) to the panchromatic imaging area. The red cross indicates the center point of HiRIC's optical FOV.

and so on [45]. HiRIC has the highest ground sample distance (GSD) of 0.5 m at 265 km, which is an effective supplement to the current submeter high-resolution Mars image data. At the same time, it can provide basic data for engineering tasks, such as landing site selection, landing site positioning, Mars surface exploration path planning for the "Zhurong" rover, and scientific tasks, such as geological background study of the landing area [26], [44].

In this article, we used the high-resolution stereo images of the "Tianwen-1" landing area acquired by HiRIC during the Mars parking orbit to produce the topographic dataset with a coverage range of 150 × 60 km by photogrammetry processing, including a digital orthophoto map (DOM) with a GSD of 0.7 and 3.5 m and the DEM with a GSD of 3.5 m. The absolute position of this dataset is in good agreement with the existing Mars topographic data, such as the CTX mosaic [6] and the HRSC/MOLA Blended DEM [8], and can present richer topographic details to meet the needs of future scientific research and engineering tasks.

II. HiRIC and Its Detection Data

A. Instrument

HiRIC adopts an off-axis three-mirror astigmatic (TMA) optical system with a focal length of 4669.794 mm, an F-number of 12, and a field of view (FOV) of 2° × 0.635°. It contains three linear-array time delay and integration charge-coupled devices (TDI CCDs) and two-area-array complementary–metal–oxide semiconductors (CMOSs) on one imaging focal plane to produce push-broom and frame imaging, respectively. TDI CCDs can work in panchromatic and four spectral bands, including blue (B1), green (B2), red (B3), and near infrared (B4), so that HiRIC can obtain both panchromatic and color images. The pixel number for the panchromatic band of each TDI CCD in the cross-scan direction is 6144 with a pixel size of 8.75 × 8.75 μm, while the pixel number for the color bands is 1536 with a pixel size of 35 × 35 μm. Each two staggered CCDs are mechanically spliced with an overlap of about 116 pixels (design value) for panchromatic band. The effective pixel number for each CMOS detector is 512 × 512 with a pixel size of 44 × 44 μm (as shown in Fig. 1 and Table I; see also [45]).

TABLE I
SPECIFICATIONS OF HiRIC

No.	Parameter name		Parameter value
1.	GSD (at the altitude of 265km)	panchromatic	>2.5m, interest areas are better than 0.5m
		colors	>10m, interest areas are better than 2.0m
2.	Field of View (FOV)		2°×0.635°
3.	F-number		12
4.	Focal length (mm)		4669.794
5.	Swath width (km, at the altitude of 265km)		9
6.	MTF（at Nyquist frequency）		＞0.18
7.	Signal- to-noise ratio (SNR, in the case of reflectance of 0.2 and solar elevation angle of 30°）		＞100
8.	Spectral wavelength (μm)	panchromatic	0.45～0.9
		colors	B1:0.45～0.52 B2:0.52～0.60 B3:0.63～0.69 B4:0.76～0.90
9.	Bits per pixel		12bit
10.	Compression		Non-compression, lossless compression, compression at 3:1/4:1/6:1/12:1/15:1

Because of the highest GSD of 0.5 m at 265 km on the Martian surface, panchromatic band CCD push-broom imaging will be the default in-orbit detection mode for HiRIC [45]. As shown in Fig. 1, the line distance along the flight direction between CCD2 and CCD1/CCD3 panchromatic band centers is 37.803 mm, while the calibrated angular distance along the flight direction between the center of the optical field view (red cross in Fig. 1) and the CCD2 and CCD1/CCD3 panchromatic band centers are 0.337° and −0.1°, respectively. It can be seen that the imaging time of the three CCDs for the same scene is significantly different. During the in-orbit detection, with the help of "Tianwen-1" orbiter flying around the Mars, HiRIC continuously images the ground targets onto the TDI CCD surface through its optical system. Through the image motion compensation calculation, adjusting the integration time and the integration levels (16–96 levels in five steps) of each CCD, the resolution of the image in the vertical and along the orbit directions can be matched, while the image motion can be controlled, so that a complete and clear image can be finally obtained, which is processed by encoding, compressing, and transmitting back to the Earth. HiRIC images are compressed using the JPEG2000 algorithm with a default compression ratio of 3:1.

B. In-Orbit Imaging Strategy and Image Acquisition

On 24 February 2021, "Tianwen-1" orbiter entered the Mars parking orbit, which is a large elliptical orbit with a periareon orbital altitude of 280 km, an apoareon orbital altitude of 59 000 km, and an orbital period of about two days. The ground track of the Mars parking orbit is almost the same in successive orbits, but its periareon will gradually shift eastward over time. When the difference in longitude between the periareon and the nominal landing site (110.318°E, 25.006°N, seen in Fig. 2) reaches 2°, periareon orbital maintenance is required. The periareon orbital arc of the Mars parking orbit transits over the landing area of "Zhurong" rover from north to south, whose center coordinates are the nominal landing site. Before the rover landed on the Mars, HiRIC performed high-resolution stereo imaging of the landing area in the periareon orbital arc. Using these stereo images, topographic dataset of the landing area was produced through photogrammetric processing within one month.

The landing area of the "Zhurong" rover is 150 km (north–south direction) × 60 km (east–west direction), as shown in Fig. 2(b). Since the imaging swath width of a single-track push-broom image is only 9 km at 265 km, to meet the demand of topographic data production, HiRIC needs to image the same area of the landing area along the north–south direction with two angles from the forward and backward views in adjacent two orbits. The imaging baseline-height ratio should be ≥0.4, i.e., the "Tianwen-1" orbiter needs to adjust ±11.31° in pitch direction for forward and backward views [Fig. 2(a)]; in addition, the overlap coverage of adjacent images along the east–west direction should be no less than 15%, so that the orbiter needs to adjust its attitude in roll direction.

Based on the analysis, we divided the landing area into nine imaging strips (Fig. 2(b); see also [45]), each with an east–west width of about 10 km and a north–south length of about 160 km, with an overlap rate of 15% between adjacent imaging strips. During the in-orbit detection, HiRIC will complete the forward- and backward-view imaging of each imaging strip one by one. Before each imaging session, according to the orbital altitude of the orbiter during its transit over the landing area, the distance of the subsatellite point of the orbiter from the center of the imaging strip and other information, the attitude angles of the orbiter in pitch and roll direction during HiRIC imaging are solved, together with its yaw angle. The orbiter attitude is controlled to align the HiRIC FOV with the imaging area, and the imaging parameters settings are completed to achieve high-resolution imaging of the imaging strips, such as integration level, image motion compensation parameters, and so on.

On 26 and 28 February 2021, test imaging sessions were conducted to verify the in-orbit operating status, image quality, and stereo imaging strategy of HiRIC. After fully verifying the data quality, HiRIC completed a total of 18 formal imaging sessions for the nine imaging strips from forward and backward views to achieve stereo coverage during 2 March to 10 April, with each imaging lasting about 42 s, imaging swath width about 11 km, and north–south length of about 170 km. Since the periareon of the Mars parking orbit shifts eastward over time and moves away from the nominal landing site, the roll angle of the orbiter is different each time HiRIC images the specified imaging strip (as shown in Table II), and the farther the periareon is from the center of the imaging strip, the larger the roll angle required for imaging. According to the analysis results of HiRIC imaging quality and the orbit determination accuracy of the "Tianwen-1" orbiter, the roll angle of the orbiter should not exceed ±20°

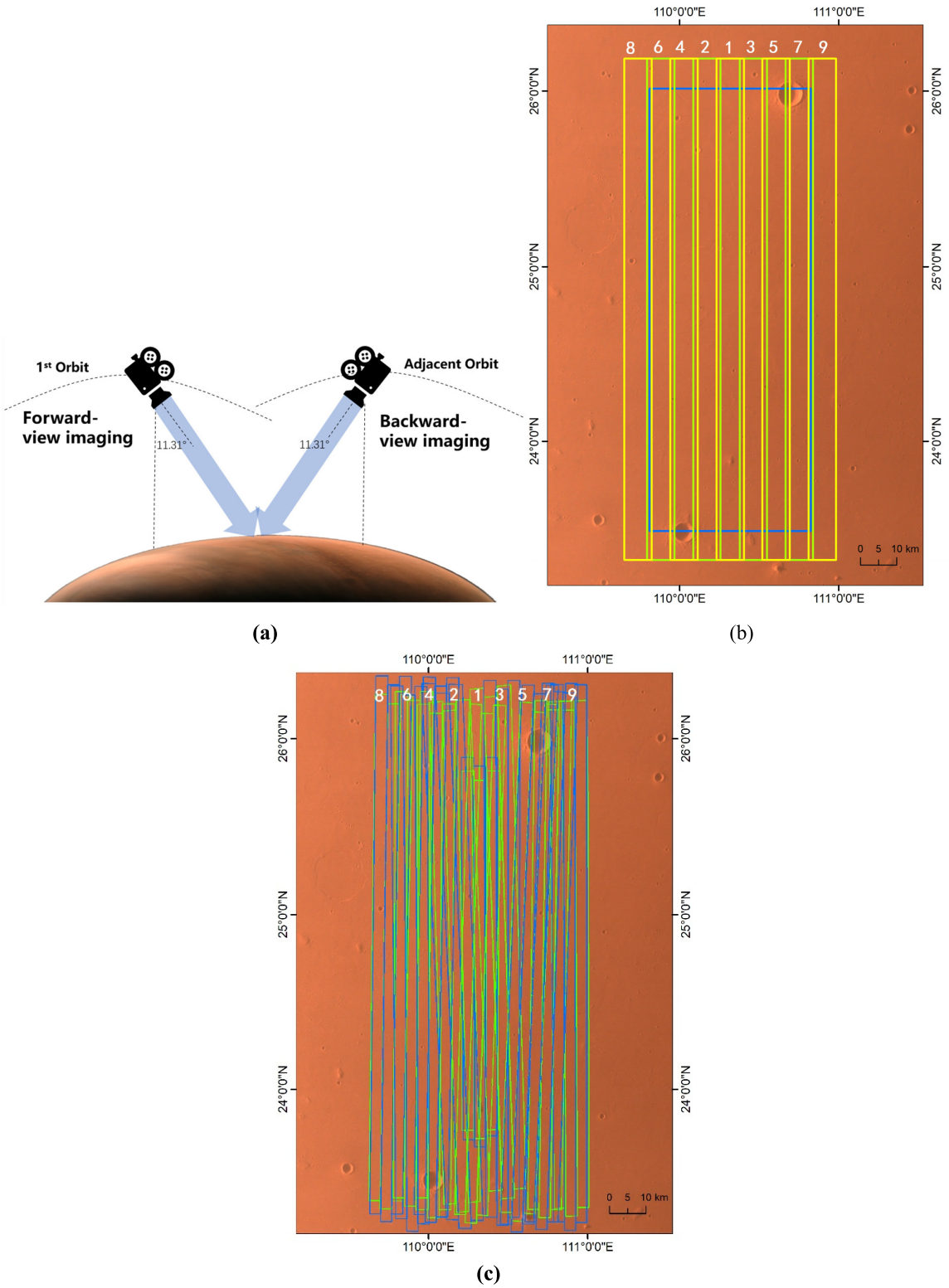

Fig. 2. Stereo coverage of "Tianwen-1" landing area by HiRIC images. (a) Stereo imaging mode of HiRIC. (b) Designed coverage of HiRIC images on the landing area. The alternating yellow and green boxes indicate nine imaging strips, numbered as 1–9 and alternated outward from the center, with an overlap coverage of 15%, and the blue box indicates the 150 km (north–south direction) × 60 km (east–west direction) landing area. (c) Actual coverage of HiRIC images obtain from 2 March to 16 April 2021, where the green and blue borders indicate the image coverage area of the forward- and backward-view images, respectively. The background image of (b) and (c) is captured by the "Tianwen-1" MoRIC, with a GSD of about 110 m.

during imaging [45], which corresponds to a 2° difference in longitude between the orbiter subsatellite points and the center of the imaging strip, beyond which the periareon orbital maintenance is required. During the Mars parking orbit stage, the orbiter has performed two periareon orbital maintenance (on 10 and 31 March, respectively); according to the locations of the periareon before and after orbital maintenance and its movement pattern, the stereo coverage of the landing area is

TABLE II
IMAGING INFORMATION FOR HiRIC

No.	Imaging time	Imaging strip	Pitch angle（° ）	Roll angle （°）	Yaw angle（° ）	Orbital altitude (km）	GSD for image strip center (m）
1.	20210302	1-forward	11.30	-2.98	2.64	351.634	0.677
2.	20210304	1-backward	-11.30	-4.25	2.54	332.529	0.642
3.	20210306	2-forward	11.30	-10.99	1.22	350.734	0.687
4.	20210308	2-backward	-11.30	-17.38	1.17	331.526	0.667
5.	20210312	3-forward	11.30	-13.99	0.93	348.105	0.689
6.	20210314	3-backward	-11.30	-4.56	2.41	329.551	0.636
7.	20210316	4-forward	11.30	-3.00	2.64	345.929	0.666
8.	20210318	4-backward	-11.30	2.17	3.16	327.982	0.632
9.	20210320	8-forward	11.30	-0.11	3.11	344.112	0.662
10.	20210322	8-backward	-11.30	0.21	2.98	326.704	0.629
11.	20210324	6-forward	11.30	-2.96	2.66	342.515	0.660
12.	20210326	6-backward	-11.30	-7.85	2.22	325.438	0.632
13.	20210328	9-forward	11.30	-7.90	1.87	340.953	0.662
14.	20210402	9-backward	-11.30	-7.02	2.33	323.246	0.626
15.	20210404	7-forward	11.30	-0.82	2.99	338.059	0.651
16.	20210406	7-backward	-11.30	6.47	3.47	321.649	0.623
17.	20210408	5-forward	11.30	7.10	4.12	336.175	0.652
18.	20210410	5-backward	-11.30	9.57	3.69	320.116	0.624
19.	20210412	1-forward 2nd coverage	11.30	3.76	3.64	334.430	0.645
20.	20210414	1-backward 2nd coverage	-11.30	0.91	3.03	318.933	0.614
21.	20210416	3-forward 2nd coverage	11.30	-4.61	2.43	332.869	0.642

achieved as an imaging order of 1, 2, 3, 4, 8, 6, 9, 7, and 5 (see Table II), which can satisfy both the consistency of the illumination conditions of each strip and the good imaging geometry conditions of the forward-view and backward-view images. Finally, between 12 and 16 April, HiRIC performed three more imaging sessions based on the coverage of the previous images. Table II presents information on the main parameters of each HiRIC imaging session since 2 March 2021.

So far, HiRIC has achieved multiview stereo coverage of the "Tianwen-1" landing area [see Fig. 2(c)], and the acquired images are clear and of the expected quality, with a GSD of 0.6–1.2 m, and image coverage meeting the topographic data production requirements. These images are all received by the ground research and application system (GRAS) of "Tianwen-1" mission through a group array of 70-m diameter antenna in Wuqing, Tianjin, 50-m diameter antenna in Miyun, Beijing, and other antennas, with a data transmission rate of up to 4 Mb/s [25]. After receiving the image data, the GRAS will carry out radiation correction, geometric positioning, and other preprocessing to generate scientific data products at all levels, which is stored in the Planetary Data System format (PDS4) and released to the public through the "Lunar and Planetary Data Release System" of GRAS (http://moon.bao.ac.cn/; see also [40]).

The level 2B data product of HiRIC images, after relative radiometric correction and geometric positioning [40], is the main data source for this article. In addition, the orbital ephemeris and attitude data of the "Tianwen-1" orbiter are used to solve the external orientation elements of the HiRIC images. The orbital ephemeris of "Tianwen-1" orbiter is provided by the Beijing Aerospace Control Center (BACC), using the J2000 coordinate system, with the precision orbiting accuracy better than 1 km (3σ) and the extrapolated orbit accuracy better than 3 km (3σ), in which the precision orbital ephemeris is used for data processing in this article; the attitude data of the orbiter are obtained by telemetry parameters, using the J2000 coordinate system too, with the measurement accuracy better than 0.05° (3σ) and the stability better than 0.0005°/s (3σ), which will cause a positional deviation of 280 m from 320-km altitude.

III. TOPOGRAPHIC DATA PROCESSING OF THE "TIANWEN-1" LANDING AREA

The original orbital ephemeris and attitude errors of the "Tianwen-1" orbiter will cause deviations in the positioning results of HiRIC images, which will affect the absolute position of the landing area topographic data. A pair of homologous points is formed between the feature points in the image and the corresponding features on the ground. Based on the geometric positioning grid file of level 2B data product, which contains the row and column coordinates of the image grid points, as well as the corresponding longitude and latitude on the Martian surface according to a sphere model with a

radius of 3396.19 km [37], the geographic coordinates of any feature point in the HiRIC image on the Martian surface can be interpolated, and ideally, the interpolated results should coincide exactly with the position of its homologous point. In this article, using the MRO CTX uncontrolled mosaic [6] with a GSD of 5 m as the planar position data and the HRSC/MOLA Blended DEM [8] with a GSD of 200 m and an elevation accuracy of ±3 m as the elevation data, the position deviation of homologous points is analyzed. About 70 homologous points were selected evenly between HiRIC images and CTX mosaic, as well as HiRIC images and HRSC/MOLA Blended DEM. The analysis results show that the average deviation of the planar position for these homologous points between HiRIC images and CTX mosaic is 1654 m (1378 pixels), which is consistent with the deviation of the planar position caused by the orbital ephemeris and attitude data accuracy level of the "Tianwen-1" orbiter, and reaches 1378 times of the original image resolution; combined with the HRSC/MOLA Blended DEM, this planar position deviation would cause an average elevation deviation of 10 m (nine pixels), which is approximately nine times the original image resolution. It should be noted that the mean CTX-to-CTX image alignment error is 150.6 m (3σ) [6] for the uncontrolled mosaic used in this article, which is large compared with the HiRIC pixel scale but small compared with the CTX-to-HiRIC alignment errors, so the CTX-to-HiRIC offsets are a reasonable estimate of the absolute error in HiRIC positions. Therefore, to achieve highly accurate topographic mapping of the "Tianwen-1" landing area, the orbital ephemeris and attitude data of the orbiter, i.e., the priori external orientation elements, need to be optimized.

Photogrammetric processing is an effective technical solution to optimize the priori external orientation elements of the image, to solve the ground coordinates of homologous points, and to ensure the high accuracy and consistency of the external orientation elements and ground point coordinates. In this article, a method for HiRIC image photogrammetry processing is studied, and high-precision topographic data of the landing area are produced.

A. Methods

In this article, HiRIC-level 2B data products were used as the main data source, and research on key photogrammetric processing techniques was carried out to produce high-precision topographic data of the landing area. First, according to the physical sensor model of HiRIC, such as geometric calibration parameters, including focal length, principal point position (internal orientation elements), splicing parameters between the three CCDs, and so on, and the orbital ephemeris and attitude data of the "Tianwen-1" orbiter (external orientation parameters), the imaging geometry model [rational function model (RFM)] of HiRIC is constructed to establish a strict geometric relationship between feature points in the HiRIC images and their corresponding Martian surface features [41]. Tie points between the forward- and backward-view images within the same imaging strip and in the overlap area between adjacent imaging strips are extracted to construct the affine transformation function between images, and then, exact matching and coarse difference rejection on the initial tie points is performed [13], [14]. These tie points are used as adjustment points for photogrammetry processing. At the same time, the CTX mosaic and the HRSC/MOLA Blended DEM mentioned earlier are used as the planer position and elevation data, respectively, to extract the adjustment control points. Uncontrolled block adjustment technology of optical remote sensing images based on "alternating direction method of multipliers (ADMM)" [4] and the global least squares adjustment method is adopted to optimize RFM model parameters and affine transformation function coefficients and to realize seamless mosaic and high precision positioning of HiRIC images. Using the optimized RMF model and affine transformation function, the epipolar line constraint relationship of the stereo image pairs is established, and the pixel-by-pixel matching of homologous points of the HiRIC forward- and backward-view stereo images is performed to obtain the dense point cloud data [47]. Inverse distance weighted (IDW) is used to produce a regular grid DEM with a GSD of 3.5 m based on the dense point cloud data. Finally, a DOM with a GSD of 3.5 and 0.7 m was produced using DEM and HiRIC images.

B. Rational Function Model

The RFM is a generalized expression of various sensor imaging geometric models, which is independent of specific sensors, simple in form, and so on. It can effectively overcome the shortcomings of traditional, strict imaging models based on colinear equations with strong correlation between orientation parameters, more solution parameters, and unstable numerical solutions, and meet the requirements of transparency of sensor parameters, generalization of imaging geometric models, and high-speed intelligence of processing, which has been widely used in sensor model calculation. The RFM is fixed based on *a priori* orientation data, and the adjustment will be done in terms of affine functions in image space.

In the RFM model of HiRIC, the relationship between image pixel coordinates and their corresponding ground coordinates is expressed by rational polynomials, where all coordinates are normalized. For descriptive convenience, let x_n and y_n be the normalized image pixel coordinates, and $(\varphi_n, \lambda_n, h_n)$ be the normalized geographic coordinates (longitude, latitude, and ellipsoidal height); then, the mathematical expression of the RFM model is as follows:

$$x_n = \mathrm{RPC}_x(\varphi_n, \lambda_n, h_n) = \frac{f_1(\varphi_n, \lambda_n, h_n)}{f_2(\varphi_n, \lambda_n, h_n)}$$
$$y_n = \mathrm{RPC}_y(\varphi_n, \lambda_n, h_n) = \frac{f_3(\varphi_n, \lambda_n, h_n)}{f_4(\varphi_n, \lambda_n, h_n)} \quad (1)$$

where $f_t(\varphi_n, \lambda_n, h_n), t = 1, 2, 3, 4$ is a cubic polynomial, which contains a total of 80 rational polynomial coefficients (RPCs; the constant term of the two denominators is fixed at 1.0) and 10 normalization parameters, which are called RPCs. The RPCs of HiRIC are computed using a topography-independent solution method proposed by Tao and Hu [41]. The method first uses the orbital attitude model of HiRIC images to establish a set of virtual 3-D grid points as control points, and then solve the RPCs by the $L2$ regularization,

which can achieve a high-precision RFM fitting of the HiRIC rigorous geometric imaging model for the subsequent photogrammetric processing.

It is important to note that the "Tianwen-1" orbiter is equipped with a total of seven scientific payloads, including HiRIC. HiRIC will share the platform with other science payloads, as well as engineering equipment, such as solar panels and high-gain antennas, all of which are sources of high-frequency vibration in HiRIC's pointing parameters. This high-frequency vibration in the stereobase direction gives rise to topographic artifacts in the form of stripes across the DEM products [22]. In addition, since the line distance along the flight direction between HiRIC's CCD2 and the CCD1/CCD3 panchromatic band centers reaches 37.803 mm, it is not possible to obtain a complete virtual image from images taken by multiple CCDs, such as the HiRISE images dose [22]. The huge difference in external orientation elements of each CCD led to the affine adjustment in image space is only a good approximation over a small region of an image. To solve the abovementioned problems, each CCD image was treated as an independent model for RPCs, and to ensure the RPC fitting accuracy, each CCD image was processed in segments with an overlap of 500 pixels (about 250 m) with each other. The imaging times of each image line in the segment were recalculated at equal intervals based on the imaging times of the first and last image lines of each image segment, and the total number of image lines in the segment. To avoid the pointing error that occurred briefly in the measured attitude over a much larger time range of the images, the design attitude of the orbiter (seen in Table II) was used instead of the measured attitude as the initial value for solving the RPCs, and the precision ephemeris and attitude corresponding to each image line were interpolated based on the imaging time after the equal-interval processing. Following the abovementioned method, all HiRIC images used here were divided into a total of 312 segments. Finally, the stable RPCs results were obtained.

C. Automated Extraction of HiRIC Images Tie Points and Control Points Considering Terrain Constraints

Obtaining accurate, evenly distributed tie and control points automatically and reliably is a key issue in the process of satellite image block adjustment. The tie points here include those between HiRIC forward- and backward-view stereo image pairs, as well as between adjacent images; for control points, since there are currently no reliable known absolute control points on the Martian surface, suitable geo-information data can be selected as the geo-referenced data, so that the problem of control points acquisition is essentially how to realize automatic registration of HiIRC images and existing geographic information data. In this article, the CTX mosaic is selected as the planar position data, and the HRSC/MOLA Blended DEM is selected as the elevation data. An automatic matching algorithm for tie points and control points is designed.

1) Enhance the texture information of images using the Wallis filter [7], [48], which is essentially a local image transformation to make the gray-scale variance and mean value at different locations in the image have approximately equal numbers, enhance the contrast of the original image as well as suppress the noise, improve the number and accuracy of feature extraction points, and increase the success rate of matching. This method can significantly improve the difficulties of image matching caused by the relatively flat terrain in the "Tianwen-1" landing area.

2) Holistic matching based on image salient edge features. The basic idea of this method is Hough transform image matching [14], that is, using the spatial geometric constraint relationship between the features extracted from HiRIC images and orthophoto images to construct affine transform functions, voting in the affine transform parameter directly for fast matching between images, which can quickly and effectively eliminate the systematic errors existing in the original RFM orientation model. The systematic errors of about several hundred or even thousands of pixels between the HiRIC images and the planar position data can be optimized to obtain a matching result of about 20–30 pixels, and finally, the tie points between the HiRIC images are obtained. The holistic matching takes only a few seconds to complete, and the matching results enable the initial positioning of HiRIC images and provide initial values for the exact matching positioning of tie and control points. The affine transformation function for an image point is given by

$$\begin{aligned} x + \Delta x &= x + a_0 + a_1 x + a_2 y = \mathrm{RPC}_x(\phi, \lambda, h) \\ y + \Delta y &= y + b_0 + b_1 x + b_2 y = \mathrm{RPC}_y(\phi, \lambda, h) \end{aligned} \quad (2)$$

where $(x,\ y)$ are the image point coordinates, and $(\Delta x,\ \Delta y)$ is their corresponding corrections, (φ, λ, h) is the 3-D coordinates of the image point on the ground, and (a_1, a_2, a_3) and (b_1, b_2, b_3) are the six affine transformation parameters for automatic extraction of tie and control points between adjacent images. For each HiRIC image, first, the Harris operator [13] is used to extract evenly distributed feature points; second, to effectively eliminate the influence of image geometric distortion caused by factors, such as terrain fluctuation, orbital position, and attitude errors on the matching results, in the automatic matching process of tie and control points, extract a feature point P on the reference image or existing geographic information data, define a matching image window W with P as the center, project the window onto a small surface element of the corresponding matching window W' on the image to be matched based on the elevation information interpolated by the DEM and the imaging model, and optimize the affine transformation parameters based on holistic matching of window W and W', and finally, the image near the predicted point in window W' is resampled and matched with the image window W in the reference image or existing geographic information data; then, the image coordinates of the points to be matched is inversed by matching results. We call this process Image-Reshaping (seen in Fig. 3). After the image matching is completed, the random sample consensus (RANSAC) algorithm [9] is used to remove the wrong matching points in the automatic matching to further improve the accuracy of image registration.

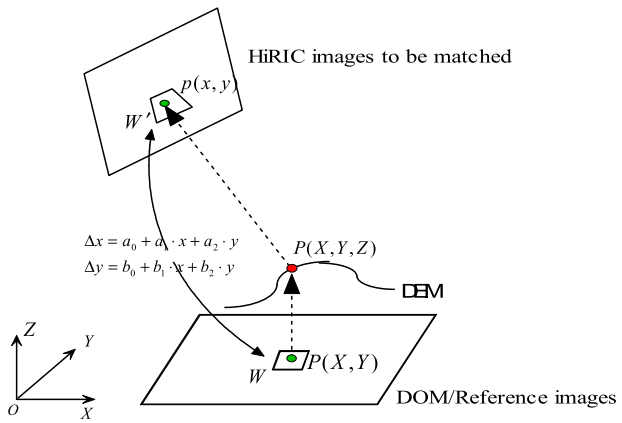

Fig. 3. Correction of geometric distortion caused by imaging geometry and topographic relief during automatic extraction of control points.

D. Uncontrolled Combined Block Adjustment

The block adjustment model based on RFM can be implemented using the RFM orientation model, and 3-D translation, affine transformation based on its model transformation. According to the image point affine transformation function [as shown in formula (2)], the block adju as follows:

$$\begin{aligned} v_{\mathrm{TP}} &= A_{\mathrm{TP}}t + B_{\mathrm{TP}}x - l_{\mathrm{TP}},\ P_{\mathrm{TP}} \\ v_{\mathrm{GCP}} &= B_{\mathrm{GCP}}x - l_{\mathrm{GCP}},\ P_{\mathrm{GCP}}. \end{aligned} \tag{3}$$

In the formula, B_{TP} and B_{GCP} represent the coefficient matrix for the ground coordinate corrections of tie and control points; A_{TP} represents the coefficient matrix for the affine transformation parameter corrections; l_{TP} and l_{GCP} represent the constant matrix of image point observations and control point observations; P_{TP} and P_{GCP} represent the weight diagonal matrix of coordinate corrections of tie and control points; t is the matrix for the affine transformation parameters corrections in the image; x is the matrix for the ground point coordinate corrections, namely

$$\begin{aligned} t &= \left[\ \Delta a_0\ \Delta a_1\ \Delta a_2\ \ \Delta b_0\ \Delta b_1\ \Delta b_2\ \right]^T \\ x &= \left[\ \Delta\varphi\ \Delta\lambda\ \Delta h\ \right]^T. \end{aligned} \tag{4}$$

Based on the least squares principle, the corresponding normal equation matrix is

$$\begin{bmatrix} A_{\mathrm{TP}}^T P_{\mathrm{TP}} A_{\mathrm{TP}} & A_{\mathrm{TP}}^T P_{\mathrm{TP}} B_{\mathrm{TP}} \\ B_{\mathrm{TP}}^T P_{\mathrm{TP}} A_{\mathrm{TP}} & B_{\mathrm{TP}}^T P_{\mathrm{TP}} B_{\mathrm{TP}} + B_{\mathrm{GCP}}^T P_{\mathrm{GCP}} B_{\mathrm{GCP}} \end{bmatrix} \begin{bmatrix} t \\ x \end{bmatrix} = \begin{bmatrix} A_{\mathrm{TP}}^T P_{\mathrm{TP}} l_{\mathrm{TP}} \\ B_{\mathrm{TP}}^T P_{\mathrm{TP}} l_{\mathrm{TP}} + B_{\mathrm{GCP}}^T P_{\mathrm{GCP}} l_{\mathrm{GCP}} \end{bmatrix}. \tag{5}$$

For the characteristics of HiRIC imaging geometry, we choose an easy-to-parallelize and efficient uncontrolled combined block adjustment method by combining the well-known "ADMM" [4] and the global least squares adjustment method in photogrammetry. The specific steps of our method are as follows.

1) Assuming that the affine transformation parameters (a_0, a_1, a_2) and (b_0, b_1, b_2) of each image are known, the ground coordinates of all tie points (φ, λ, h) can be calculated, which is called "forward intersection," and the normal equation for each tie point is only a 3×3 matrix.

2) Assuming that the ground coordinates (φ, λ, h) of all tie points are known, the affine transformation parameters (a_0, a_1, a_2) and (b_0, b_1, b_2) of each image can be calculated, which is called "backward intersection," and the normal equation of this step is only a 6×6 matrix for each image.

3) Repeat 1) and 2) until the iterative change of all unknowns is less than a predefined threshold to obtain the optimal initial values of all unknowns.

4) Using the image affine transformation parameters and the tie point ground coordinates, the image residuals $(v_x, v_y)_{i,i=1,2,\ldots,n}$ of all tie points can be calculated, where n means that the tie point appears in the n-view images. Let $v_i = \mathrm{sqrt}(v_x^2 + v_y^2)$, and $v_{\max} = \max(v_{i,i=1,2,\ldots,n})$, and set *a priori* weight of $p = 1.0/v_{\max}^2$ for each tie point.

5) Based on the ground coordinates of the tie points and the corresponding *a priori* weights, the global least-squares adjustment for RFM parameters is executed based on (1)–(4), and the small-scale gross errors that still exist are removed by the iterative weight of tie points calculated based on their image residuals after adjustment.

In the uncontrolled adjustment method proposed in this article, an "average" virtual control point is constructed by the "ADMM" to solve the ill-conditioned (rank deficient) problem of the normal equation matrix encountered in the uncontrolled adjustment. On the one hand, this method can use parallel computation to quickly calculate the initial values of the unknowns to be adjusted, and on the other hand, it also uses the "good" initial values to finally perform the least squares overall adjustment.

E. Dense Point Cloud Matching Based on Multi-Image and Multifeature Matching Algorithm

A dense, accurate, and reliable high-precision dense point cloud matching algorithm for linear-array images is the key to generating DEM data. In this article, a multi-image correlation matching algorithm (geometrically constrained cross correlation (GC3) [47] is proposed based on 3-D geometric constraints for HiRIC linear-array images on the basis of the traditional image correlation matching algorithm. The algorithm can organically combine the matching results of various matching elements (feature points, feature lines, and grid points) and make full use of the local and global texture information of the image, so that the automatically matched feature points and lines can fully express the important features of the topography, which can be applied to the dense grid point matching in the area without texture or with little texture to meet the requirements of Mars image data processing.

In the dense point cloud matching process, one of the several images is selected as the reference image, and the others are all images to be matched. Using the Image-Reshaping introduced earlier, we can obtain the matching results of the reference image feature points on the search image pixel by pixel using the precise orientation parameters obtained after block adjustment. Similarly, distortions caused by the terrain undulation, imaging geometry, and imaging scale can be automatically compensated during the image matching process.

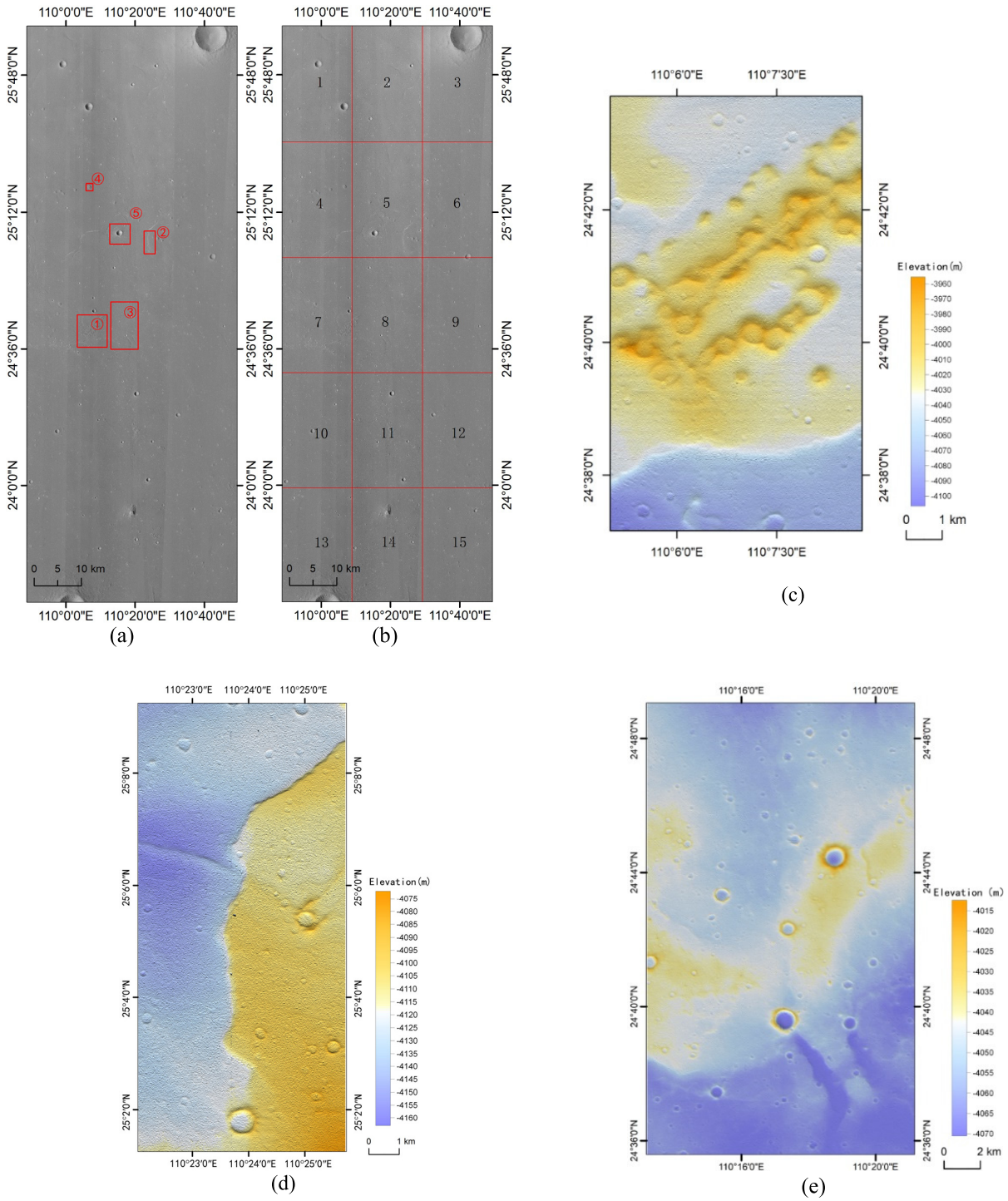

Fig. 4. Topographic dataset of "Tianwen-1" landing area. (a) DOM with a GSD of 3.5 m and covering an area of 150 × 60 km. (b) Subframe grid of the DOM with a GSD of 0.7 m. (c)–(e) DEM details of the local area of the "Tianwen-1" landing area, with a GSD of 3.5 m, and their locations are marked as ①–③, respectively, in (a), showing the landing area features, such as suspected mud volcanoes, wrinkled ridges, craters, and so on. Based on the scale bar, it can be seen that the smallest craters identifiable in the DEM produced in this article are about 50 m in diameter.

IV. Topography of "Tianwen-1" Landing Area and Accuracy Analysis

In this article, a high precision topographic dataset of the "Tianwen-1" landing area with a range of 150 × 60 km, including DOM and DEM, was produced using the HiRIC high-resolution stereo images during the Mars parking orbit through photogrammetry processing, taking CTX mosaic as the planar position data and the HRSC/MOLA Blended DEM as the elevation data. The DOMs include two types of products with a GSD of 0.7 and 3.5 m, respectively, and the GSD of the DEM product is 3.5 m. The DOM product with 0.7-m GSD has a total of 15 subframe products, and each subframe covers a range of 30 × 20 km, with an overlap of ten pixels between adjacent subframes (as shown in Fig. 4).

TABLE III
TOPOGRAPHIC DATASET OF "TIANWEN-1" LANDING AREA

Product	Projection	Reference ellipsoid	Spatial resolution	Images	File format	Data amount
Sub-frame DOMs	equidistant cylindrical projection	sphere with a radius of 3396.19 km	0.7m	15	GeoTIFF	17.10 GB
DOM			3.5m	1	GeoTIFF	311 MB
DEM			3.5m	1	GeoTIFF	1.23 GB

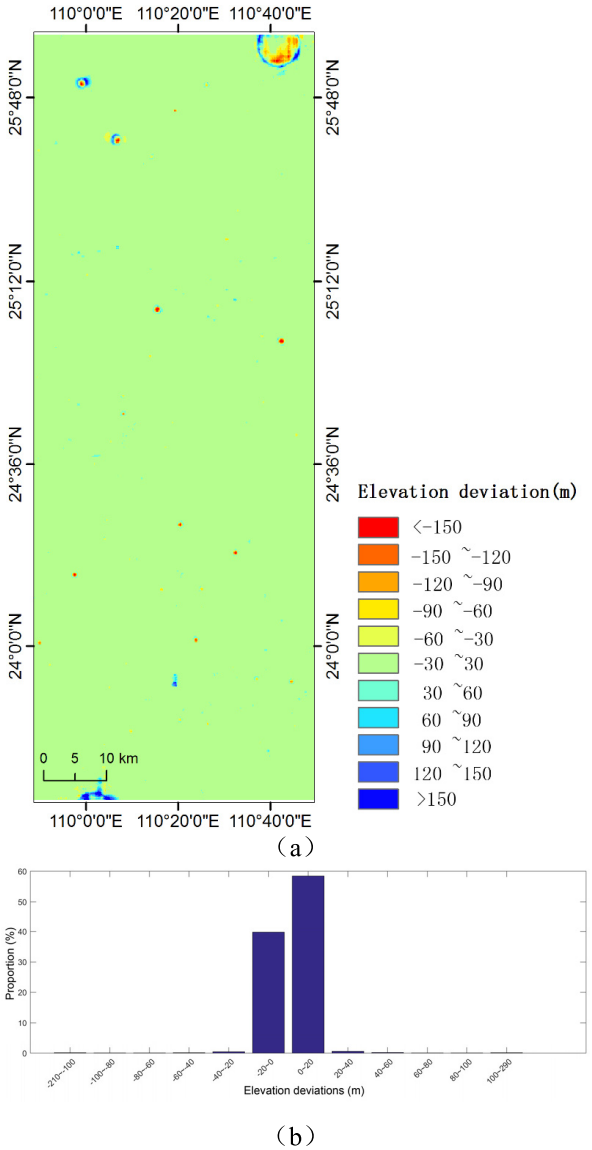

Fig. 5. Elevation deviation between our DEM data and MOLA topographic data in the "Tianwen-1" landing area. (a) Spatial distribution of elevation deviations. (b) Corresponding error histogram.

Table III gives the main information of this topographic dataset, which uses a equidistant cylindrical projection with the Mars fixed coordinate system as the reference system, which takes the center of mass of Mars as the origin, a sphere with a radius of 3396.19 km as the reference ellipsoid, the equatorial plane of Mars as the reference plane, and the X-, Y-, and Z-axes are parallel to the corresponding three axes of the fixed

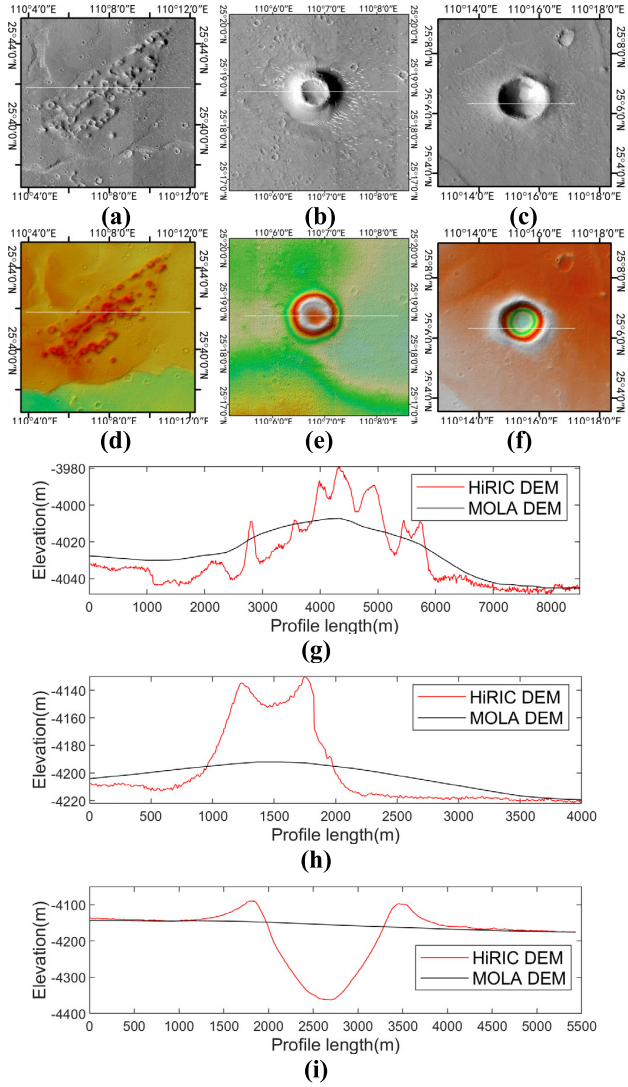

Fig. 6. Topographic details in "Tianwen-1" landing area. (a)–(c) DOM of typical landforms, including cones, craters, suspected mud volcanoes, and so on, whose locations are marked as ①, ④, and ⑤ in Fig 4(a). (d)–(f) Corresponding DEM. (g)–(i) Elevation value corresponding to the profile lines in (a)–(c) from the DEM of this work and the HRSC/MOLA Blended DEM, respectively.

coordinate system based on the International Astronomical Union (IAU) orientation parameter model [37].

The GSD of the landing area topographic dataset produced in this article is about 60 times higher than that of the HRSC/MOLA Blended DEM (with a GSD of 200 m), which can present more abundant topographic details [as shown in Fig. 4(c)–(e)], effectively support the landing site positioning of the "ZhuRong" rover, and provide important basic data for the remote operation planning of the rover on the Martian surface and its scientific detection planning [26]. This topographic dataset has already been released through the "Lunar and Planetary Data Release System." The following is an analysis of the precision of the "Tianwen-1" landing area topographic dataset.

A. Adjustment Precision

The positional deviation between the inverse projection position and its actual position of adjustment points in the

TABLE IV
STATISTICS OF NETWORK ADJUSTMENT RESULTS FOR HiRIC IMAGES (WITHIN IMAGING STRIPS)

Imaging strips	Imaging No.	Adjustment points	Pixel residuals (RMS pixels)	Control points	Control points deviation RMS（m）	Tie points between adjacent strip	Pixel residuals (RMS pixels)
1	1/2	414327	0.53	22	2.838	39276	0.79
2	3/4	371198	0.43	36	0.536	33334	0.64
3	5/6	295489	0.40	57	1.347	32687	0.60
4	7/8	358251	0.46	41	0.348	33085	0.69
5	17/18	303452	0.58	37	4.159	35220	0.87
6	11/12	400962	0.42	28	1.507	39090	0.63
7	15/16	380847	0.42	33	1.957	34902	0.63
8	9/10	317210	0.57	37	1.494	37335	0.86
9	13/14	429504	0.43	25	3.432	40402	0.64
1-backup	19/20	378543	0.48	24	1.451	26855	0.72
3-backup	21/6	158567	0.48	131	3.240	28645	0.72
Average value	/	/	0.47	/	20.28	/	0.71

NOTE: THE IMAGING NO. CORRESPONDS TO THE 21 IMAGING OF HiRIC LISTED IN TABLE 2.

image after block adjustment, i.e., the pixel residuals, reflects the adjustment precision. During the photogrammetry process in this article, the number of adjustment points within each imaging strip during photogrammetry exceeds 100 000, and the ones between adjacent strips exceeds 30 000 on average (seen in Table IV), with a matching accuracy of about 0.1 pixel (rms). The point automatic matching algorithm is correct and effective.

Table IV shows the pixel residuals of adjustment points within and between 11 stereo imaging strips during the production of the landing area topographic dataset. It can be seen that the standard deviation of the pixel residuals for adjustment points within stereo imaging strips is less than 0.6 pixels, and the average value is 0.47 pixels. This deviation reflects the random error of the HiRIC imaging model established after block adjustment (without considering other factors) in the calculation of the 3-D coordinates of adjustment point on the Martian surface, corresponding to a standard deviation of about 1.0 m for the elevation error and 0.4 m for the planar position error. The average value of the standard deviation of control point position is 2.02 m, which is consistent with the error of the 3-D coordinates reflected by pixel residuals of image points. On the other hand, the 11 stereo image pairs adopt the same planar position and elevation data, so that the pixel residuals of adjustment points between subtopographic data are less than 0.9 pixels, which realizes seamless mosaic of the final complete topographic dataset. The error statistics indicate that the internal consistency of the topographic dataset is good, and the adjustment process works well.

B. Cross Validation for the Positional Precision

In this article, the positional precision of "Tianwen-1" landing area topographic data is analyzed by cross validating with CTX mosaic and HRSC/MOLA Blended DEM.

For the planar position precision, 36 evenly distributed checkpoints were selected from the "Tianwen-1" landing area DOM and compared with the planar position at the corresponding checkpoints in CTX mosaic. The results show that the average planar position deviation between the "Tianwen-1" landing area DOM and CTX mosaic is 24 m, with an rms value of 15 m. It can be noted that a deviation of 15 m is much larger than the control points standard deviations. The reason is that, on the one hand, there would be a certain matching error, because check points were manually extracted; on the other hand, only the feature points with small horizontal deviation are retained as control in the adjustment process. The position precision of the control points reflects the internal consistency of the topographic dataset, while the position precision of the check points reflects the actual position deviation between the topographic dataset and the existing terrain data. The precision analysis shows that although the CTX dataset is an uncontrolled mosaic, "Tianwen-1" landing area topographic dataset registers well to the control source, which indicates that our implementation works at the indicated level of precision and accuracies on this order can reasonably be expected if a more accurate control source is used.

For the elevation precision, the DEM of the landing area was resampled to a spatial resolution of 200 m and subtracted from the HRSC/MOLA Blended DEM to analyze the elevation deviation between them. The results show that the average elevation deviation between "Tianwen-1" landing area DEM and the HRSC/MOLA Blended DEM is −7 m with an rms value of 10 m, in which the deviation in 95.70% of the area is less than 10 m (seen in Fig. 5). It should be noted that the actual resolution of the HRSC/MOLA Blended DEM is poorer than 200 m because of the large gaps between altimetry profiles. Comparing the DOM of the landing area [seen in Fig. 4(a)], it can be seen that the areas with larger deviation are mainly concentrated in the bottom of craters, the boundary of the suspected volcanoes, and so on, which is caused by the large spatial resolution difference between the two types of topographic data. The positional deviation statistics are shown in Table V.

TABLE V
STATISTICS OF LANDING AREA TERRAIN DATASET LOCATION PRECISION

	maximum value（m）	minimum value（m）	mean value (m)	RMS（m）
planar position deviation for checkpoints	82	9	24	15
elevation deviation	289	-209	-6	10
elevation deviation (excluding the bottom of craters, suspected mud volcanoes and other areas)	32	-28	-2	2

Therefore, the "Tianwen-1" landing area topographic dataset produced in this article is in good consistency with the existing Mars topographic data in terms of positional precision and has obvious advantages in terms of spatial resolution and topographic detail expression. As seen in Fig. 6, compared with the HRSC/MOLA Blended DEM, the topographic dataset produced in this article can clearly and accurately present topographic details, such as the distribution of suspected mud volcanoes, the top depression of the cone, the pit wall of the crater, and other topographic features with the dimensions of less than 100 m and a minimum of about 15 times the DEM grid spacing, which can be used to accurately measure the topographic parameters, such as the diameter, depth, and slope of the craters.

V. CONCLUSION

HiRIC is another high-resolution optical camera for Mars exploration mission, with the highest GSD up to 0.5 m at 265 km, and its detection data are an effective supplement to the current submeter-level high-resolution images on the Martian surface. In this article, an in-orbit stereo imaging strategy was designed based on the characteristics of HiRIC, and the photogrammetry processing was carried out using 21 high-resolution stereo images of the landing area acquired by HiRIC during the Mars parking orbit, focusing on key technologies, such as camera imaging geometry model construction, extraction of tie and control points considering terrain constraints, combined block adjustment under uncontrolled conditions, and dense pixel-by-pixel matching of multiview images. The topographic dataset of the "Tianwen-1" landing area was produced, including the DOM with a GSD of 3.5 and 0.7 m and the DEM with a GSD of 3.5 m.

Statistical analysis shows that the standard deviation of the pixel residuals for adjustment points within and between image strips during the photogrammetry processing is better than one pixel, which greatly improves the positioning precision of original images and realizes the seamless mosaic of the topographic dataset in the landing area. In terms of planar position and elevation, our topographic dataset has a good consistency with the existing Martian topographic data, such as CTX mosaic and HRSC/MOLA Blended DEM, and can present abundant topographic details due to the GSD of 3.5 m.

At present, the "Tianwen-1" orbiter is conducting the global remote sensing exploration, and the main task is to achieve global coverage of Martian surface using the moderate-resolution imaging camera (MoRIC), during which the HiRIC mainly performs high-resolution imaging of typical terrain and landforms on the Martian surface, such as valleys, volcanoes, craters, and so on. Because HiRIC stereo coverage requires frequent adjustment of the orbiter attitude, to ensure the global remote sensing exploration mission, currently, no HiRIC stereo images are acquired again for the time being. After the end of the global remote sensing exploration mission, stereo imaging will be arranged according to the exploration requirement during the extended mission to supplement the stereo coverage area of meter-scale high-resolution images on the Martian surface. In addition, due to the acquisition of high-resolution images of different seasons and different geographical locations, HiRIC is also expected to provide basic data for the solution of atmospheric correction, dust elimination, photometric correction, color correction, and other problems [5], [18], [19], [32] in Mars high-resolution images.

In summary, the topographic dataset produced in this article has achieved seamless mosaic and high-precision positioning within the "Tianwen-1" landing area. It has been applied in scientific and engineering missions, such as the geological background study of the landing area, the positioning of the "Zhurong" rover landing site, and the Martian surface remote operation planning of the rover.

REFERENCES

[1] J. Albertz *et al.*, "HRSC on Mars Express—Photogrammetric and cartographic research," *Photogramm. Eng. Remote Sens.*, vol. 71, no. 10, pp. 1153–1166, 2005.
[2] F. S. Anderson and T. J. Parker, "Characterization of MER landing sites using MOC and MOLA," in *Proc. 33rd Lunar Planet. Sci. Conf.*, League City, TX, USA, Mar. 2002, p. 20020045549.
[3] B. A. Archinal *et al.*, "A new Mars digital image model (MDIM 2.1) control network," *Int. Arch. Photogramm. Remote Sens.*, vol. 35, pp. 863–868, Apr. 2004.
[4] S. Boyd, "Distributed optimization and statistical learning via the alternating direction method of multipliers," *Found. Trends Mach. Learn.*, vol. 3, no. 1, pp. 1–122, 2010.
[5] W. A. Delamere *et al.*, "Colour imaging of Mars by the high resolution imaging science experiment (HiRISE)," *Icarus*, vol. 205, pp. 38–52, Jan. 2010.
[6] J. L. Dickson *et al.*, "The global CTX mosaic of mars: Lessons for the construction and dissemination of massive imaging data sets," in *Proc. 51st Lunar Planetary Sci. Conf.*, 2020, p. 2309.
[7] C. Fan, X. Chen, L. Zhong, M. Zhou, Y. Shi, and Y. Duan, "Improved Wallis dodging algorithm for large-scale super-resolution reconstruction remote sensing images," *Sensors*, vol. 17, no. 3, p. 623, Mar. 2017, doi: 10.3390/s17030623.
[8] R. L. Fergason, T. M. Hare, and J. Laura, "HRSC and MOLA blended digital elevation model at 200m v2," in *Astrogeology PDS Annex, U.S. Geological Survey*. Flagstaff, AZ, USA: USGS Astrogeology Science Center, 2018. [Online]. Available: http://bit.ly/HRSC_MOLA_Blend_v0
[9] M. Fischler and R. Bolles, "Random sample consensus: A paradigm for model fitting with applications to image analysis and automated cartography," *Commun. ACM*, vol. 6, no. 24, pp. 381–395, 1981.
[10] K. Gwinner *et al.*, "Derivation and validation of high-resolution digital terrain models from Mars Express HRSC-data," *Photogramm. Eng. Remote Sens.*, vol. 75, no. 9, pp. 1127–1142, 2009.
[11] K. Gwinner *et al.*, "The first quadrangle of the Mars Express HRSC multi orbit data products (MC-11-e)," in *Proc. ISPRS Workshop Commission*, 2015.
[12] K. Gwinner *et al.*, "The high resolution stereo camera (HRSC) of Mars Express and its approach to science analysis and mapping for Mars and its satellites," *Planet. Space Sci.*, vol. 126, pp. 93–138, Jul. 2016, doi: 10.1016/j.pss.2016.02.014.
[13] C. Harris and M. Stephens, "A combined corner and edge detector," in *Proc. Alvey Vis. Conf.*, 1988, p. 15.

[14] P. E. Hart, "How the Hough transform was invented," *IEEE Signal Process. Mag.*, vol. 26, no. 6, pp. 18–22, Oct. 2009.
[15] R. Jaumann, "The high resolution stereo camera (HRSC) experiment on Mars Express: Instrument aspects and experiment conduct from interplanetary cruise through the nominal mission," *Planet. Space Sci.*, vol. 55, nos. 7–8, pp. 928–952, 2007.
[16] L. Keszthelyi *et al.*, "High resolution imaging science experiment (HiRISE) images of volcanic terrains from the first 6 months of the Mars Reconnaissance Orbiter primary science phase," *J. Geophys. Res., Planets*, vol. 113, no. E4, 2008, Art. no. E04005.
[17] J. R. Kim and J.-P. Müller, "Multi-resolution topographic data extraction from Martian stereo imagery," *Planet. Space Sci.*, vol. 57, nos. 14–15, pp. 2095–2112, Dec. 2009, doi: 10.1016/j.pss.2009.09.024.
[18] R. L. Kirk *et al.*, "Photometric modeling for planetary cartography," in *Proc. 31rd Lunar Planet. Sci. Conf.*, 2000, p. 2025.
[19] R. L. Kirk, K. T. Thompson, and E. M. Lee, "Photometry of the Martian atmosphere: An improved practical model for cartography and photoclinometry photometric modeling for planetary cartography," in *Proc. 32rd Lunar Planetary Sci. Conf.*, 2001, p. 1874.
[20] R. L. Kirk *et al.*, "High-resolution topomapping of candidate MER landing sites with Mars orbiter camera narrow-angle images," *J. Geophys. Res.*, vol. 108, no. E12, p. 8088, 2003.
[21] R. L. Kirk, J. M. Barrett, and L. A. Soderblom, "Photoclinometry made simple. . .? Paper presented as ISPRS-ET working group IV," in *Proc. Int. Soc. Photogramm. Remote Sens.*, Houston, TX, USA, 2003.
[22] R. L. Kirk *et al.*, "Ultrahigh resolution topographic mapping of Mars with MRO HiRISE stereo images: Meter-scale slopes of candidate Phoenix landing sites," *J. Geophys. Res., Planets*, vol. 113, pp. 1–31, Jun. 2008, Art. no. E00A24.
[23] R. L. Kirk, E. Howington-Kraus, and K. Edmundson, "Community tools for cartographic and photogrammetric processing of Mars Express HRSC images," in *Planetary Remote Sensing and Mapping*, B. Wu, K. Di, J. Oberst, and I. Karatschevseva, Eds. New York, NY, USA: Taylor & Francis, 2018, pp. 107–124, doi: 10.1201/9780429505997.
[24] R. L. Kirk *et al.*, "Evaluating stereo digital terrain model quality at Mars rover landing sites with HRSC, CTX, and HiRISE images," *Remote Sens.*, vol. 13, no. 17, p. 3511, Sep. 2021, doi: 10.3390/rs13173511.
[25] C. Li *et al.*, "China's Mars exploration mission and science investigation," *Space Sci. Rev.*, vol. 217, p. 57, Apr. 2021.
[26] J. Liu *et al.*, "Geomorphic contexts and science focus of the Zhurong landing site on Mars," *Nature Astron.*, vol. 6, no. 1, pp. 65–71, Jan. 2022, doi: 10.1038/s41550-021-01519-5.
[27] M. C. Malin *et al.*, "Mars observer camera," *J. Geophys. Res.*, vol. 97, no. E5, p. 7699, 1992.
[28] M. C. Malin *et al.*, "Context camera investigation on board the Mars reconnaissance orbiter," *J. Geophys. Res.*, vol. 112, Jun. 2007, Art. no. E05S04.
[29] M. C. Malin *et al.*, "An overview of the 1985–2006 Mars orbiter camera science investigation," *Mars*, vol. 5, pp. 1–60, Jan. 2010.
[30] A. McEwen *et al.*, "Mars reconnaissance orbiter's high resolution imaging science experiment (HiRISE)," *J. Geophys. Res.*, vol. 112, May 2007, Art. no. E05S02.
[31] A. McEwen *et al.*, "The high resolution imaging science experiment (HiRISE) during MRO's primary science phase (PSP)," *Icarus*, vol. 205, pp. 2–37, Apr. 2010.
[32] T. B. McCord *et al.*, "Mars express high resolution stereo camera spectrophotometric data: Characteristics and science analysis," *J. Geophys. Res., Planets*, vol. 112, Jun. 2007, Art. no. E06004.
[33] MSSS (Malin Space Science System). (2002). *Mars Global Surveyor Mars Orbiter Camera Geodesy Campaign Mosaic*. [Online]. Available: http://www.msss.com/mgcwg/mgm/
[34] G. Neukum and R. Jaumann, "The high resolution stereo camera of Mars express," *Mars Exp., Sci. Payload*, vol. 1240, pp. 17–35, Aug. 2004.
[35] J. Oberst *et al.*, "The imaging performance of the SRC on Mars express," *Planet. Space Sci.*, vol. 56, nos. 3–4, pp. 473–491, Mar. 2008.
[36] M. S. Robinson *et al.*, "Lunar reconnaissance orbiter camera (LROC) instrument overview," *Space Sci. Rev.*, vol. 150, nos. 1–4, pp. 81–124, Jan. 2010.
[37] M. E. Davies *et al.*, "Report of the IAU/IAG/COSPAR working group on cartographic coordinates and rotational elements of the planets and satellites: 1985," *Celestial Mech.*, vol. 39, no. 1, pp. 103–113, May 1986.
[38] M. Spiegel, "Improvement of interior and exterior orientation of the three line camera HRSC with a simultaneous adjustment," *Int. Arch. Photogramm. Remote Sens. Spat. Inf. Sci.*, vol. 36, pp. 161–166, May 2007.
[39] D. E. Smith *et al.*, "Mars orbiter laser altimeter-experiment summary after the first year of global mapping of Mars," *J. Geophys. Res.*, vol. 106, no. E10, pp. 23689–23722, 2001.
[40] X. Tan *et al.*, "Design and validation of the scientific data products for China's Tianwen-1 mission," *Space Sci. Rev.*, vol. 217, p. 69, May 2021.
[41] C. V. Tao and Y. Hu, "A comprehensive study of the rational function model for photogrammetric processing," *Photogramm. Eng. Remote Sens.*, vol. 67, no. 12, pp. 1347–1357, Dec. 2001.
[42] N. Thomas *et al.*, "The colour and stereo surface imaging system (CaSSIS) for the ExoMars trace gas orbiter," *Space Sci. Rev.*, vol. 212, pp. 1897–1944, Jun. 2017.
[43] USGS. (2014). *Mars Viking Colorized Global Mosaic 232m V2*. [Online]. Available: https://astrogeology.usgs.gov/search/map/Mars/Viking/MDIM21/Mars_Viking_MDIM21_ClrMosaic_global_232m
[44] B. Wu *et al.*, "Landing site selection and characterization of Tianwen-1 (Zhurong Rover) on Mars," *J. Geophys. Res., Planets*, vol. 127, no. 4, pp. 1–17, Apr. 2022, Art. no. e2021JE007137, doi: 10.1029/2021JE007137.
[45] W. Yan *et al.*, "Detection capability verification and performance test for the high resolution imaging camera of China's Tianwen-1 mission," *Space Sci. Rev.*, vol. 217, p. 71, Jun. 2021.
[46] J.-S. Yoon and J. Shan, "Combined adjustment of MOC stereo imagery and MOLA altimetry data," *Photogramm. Eng. Remote Sens.*, vol. 71, no. 10, pp. 1179–1186, 2005.
[47] Z. Li, *Automatic Digital Surface Model (DSM) Generation From Linear Array Images*. Zurich, Switzerland: Swiss Federal Institute of Technology, 2005, pp. 81–85.
[48] Z. Li, Z. Zuxun, and Z. Jianqing, "The image matching based on Wallis filtering," *Geomatics Inf. Sci. Wuhan Univ.*, vol. 24, no. 1, pp. 24–27 and 35, 1999.

Wei Yan received the B.S. and Ph.D. degrees from Wuhan University, Wuhan, China, in 2006 and 2012, respectively.

He is currently with the National Astronomical Observatories, Chinese Academy of Sciences (CAS) and with the School of Astronomy and Space Science, University of Chinese Academy of Sciences, Beijing, China. His research interests include lunar exploration and planetary remote sensing for China Lunar and Mars exploration.

Xin Ren received the B.S. degree in surveying and mapping from Wuhan University, Wuhan, China, in 2001, the M.S. degree in cartography and geographic information system from the Institute of Remote Sensing Application, Chinese Academy of Sciences (CAS), Beijing, China, in 2004, and the Ph.D. degree in astronomical of techniques and methodology from the National Astronomical Observatories, CAS, in 2011.

He is currently a Professor with the National Astronomical Observatories, CAS, and a Teacher with the School of Astronomy and Space Science, University of Chinese Academy of Sciences, Beijing. His research interests include planetary exploration data preprocessing, planetary remote sensing and mapping, and photogrammetry.

Jianjun Liu received the B.S. degree from Jiangxi Normal University, Nanchang, China, in 1997, and the Ph.D. degree from the Institute of Geochemistry, Chinese Academy of Sciences (CAS), Beijing, China, in 2002.

He participated in several China National Space Administration's (CNSA's) lunar and deep-space exploration missions with major roles, including Chang'E-1 mission (CE-1), Chang'E-2 mission (CE-2), Chang'E-3 mission (CE-3), and the ongoing mission. He is currently a Professor with the National Astronomical Observatories, CAS, and a Teacher with the School of Astronomy and Space Science, University of Chinese Academy of Sciences, Beijing. His research interests include planetary remote sensing and cartography, planetary morphology, and planetary surface processes.

Li Zhang received the Ph.D. degree from the Swiss Federal Institute of Technology in Zürich (ETH Zürich), Zürich, Switzerland, in 2005.

He is currently a full-time Professor with the Chinese Academy of Surveying and Mapping (CASM), Beijing, China. His research interests include digital photogrammetry, computer vision, optical and SAR satellite image processing, and multisource spatial data fusion.

Wangli Chen received the B.S. degree from Central South University, Changsha, China, in 2008, and the Ph.D. degree from Wuhan University, Wuhan, China, in 2015.

She was with the National Astronomical Observatories, Chinese Academy of Sciences (CAS), Beijing, China. She is involved in remote sensing image processing. Her research interests include image matching and 3-D reconstruction.

Dong Wang received the Ph.D. degree from the University of Chinese Academy of Sciences, Changchun, China, in 2007.

He is currently with the Changchun Institute of Optics, Fine Mechanics and Physics, Chinese Academy of Sciences (CAS), Changchun. His research interests include integrated design for space optical instrument and processing of remote sensing image data.

Qiang Fu received the B.S. and M.S. degrees from Beihang University, Beijing, China, in 2005 and 2008, respectively.

He is currently with the National Astronomical Observatories, Chinese Academy of Sciences (CAS), Beijing. His research interests include detector payload operation management for China Lunar and Mars exploration.

Xu Tan received the B.S. degree from the Shandong University of Technology, Shandong, China, in 2006, and the Ph.D. degree from the National Astronomical Observatories, Chinese Academy of Sciences (CAS), Beijing, China, in 2015.

She is currently with the National Astronomical Observatories, CAS. Her research interests include planetary science and data processing.

Xiaoxia Zhang received the B.S. and master's degrees from the Beijing Institute of Technology, Beijing, China, in 2008 and 2010, respectively.

She is currently with the National Astronomical Observatories, Chinese Academy of Sciences, Beijing. Her research interests include data processing and data quality evaluation.

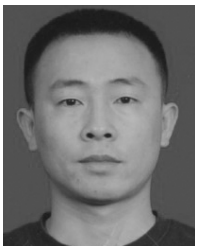

Haibin Ai received the Ph.D. degree from Wuhan University, Wuhan, China, in 2009.

He is currently a full-time Professor with the Chinese Academy of Surveying and Mapping (CASM), Beijing, China. His research interests include digital photogrammetry, computer vision, and optical satellite image processing.

Baoqian Wang received the M.S. degree from the China University of Geosciences (Beijing), Beijing, China, in 2013.

He is currently an Assistant Research Fellow with the Chinese Academy of Surveying and Mapping (CASM), Beijing. His research interests include digital photogrammetry and optical satellite image processing.

Quanquan Zhi received the M.S. degree from Tsinghua University, Beijing, China, in 2015.

He is currently with the Beijing Aerospace Control Center (BACC), Beijing. His research interests include space tracking, telemetry and control (TT&C) and operation management for China Mars and Lunar exploration.

Zichen Huang received the B.S. degree from Shanghai Jiaotong University, Shanghai, China, in 2015, and the M.S. degree from Space Engineering University, Beijing, China, in 2018.

He is currently with the Beijing Aerospace Control Center (BACC), Beijing. His research interests include mission planning and TT&C for China Mars and Lunar exploration.

Chen Song received the B.S. and M.S. degrees from the National University of Defense Technology, Changsha, China, in 2016 and 2018, respectively.

He is currently with the Beijing Aerospace Control Center (BACC), Beijing, China. His research interests include orbit determination for China Mars exploration.